Journal of Hydrology 621 (2023) 129667

Contents lists available at ScienceDirect

Journal of Hydrology

journal homepage: www.elsevier.com/locate/jhydrol

Research papers

Joint assimilation of satellite soil moisture and streamflow data for the hydrological application of a two-dimensional shallow water model

G. García-Alén [a,*], R. Hostache [b], L. Cea [a], J. Puertas [a]

[a] Universidade da Coruña, Water and Environmental Engineering Group, Center for Technological Innovation in Construction and Civil Engineering (CITEEC), Campus de Elviña, A Coruña 15071, Spain
[b] UMR Espace-Dev, IRD, Univ. Réunion, Univ. Guyane, Univ. Antilles, Univ. Nouvelle Calédonie, UPVD, Univ. Montpellier, Montpellier, France

ARTICLE INFO

Keywords:
Hydrodynamic modelling
Iber+
Flood forecasting
Tempered particle filter
Shallow water equations
Data assimilation

ABSTRACT

Data assimilation (DA) in physically-based hydrodynamic models is conditioned by the difference in temporal and spatial scales of the observed data and the resolution of the model itself. In order to use remote sensing data in small-scale hydrodynamic modelling, it is necessary to explore innovative DA methods that can lead to a more plausible representation of the spatial variability of the parameters and processes involved. In the present study, satellite-derived soil moisture and in situ-observed streamflow data were jointly assimilated into a high-resolution hydrological-hydrodynamic model based on the Iber software, using the Tempered Particle Filter (TPF) for the dual estimation of model state variables and parameters. Twelve storm events occurring in a 199 km^2 catchment located in NW Spain were used for testing the proposed approach. A 3-step procedure was followed: (1) sensitivity analysis of the model parameters; (2) joint assimilation of soil moisture and discharge data to estimate correlations between observations and model parameters; (3) joint assimilation of soil moisture and discharge data using an initial set of particles and parameter standard deviations derived from prior information. The numerical model correctly reproduces the observed data, with an average Nash-Sutcliffe efficiency (NSE) value of 0.74 over the 12 events when the prior information is used. The approach described is shown to be most efficient with storm events that produce isolated peak discharges.

1. Introduction

The inherent uncertainty of hydrological modelling (Blöschl et al., 2019) can be reduced by assimilating independent observed data, such as satellite observations or data from gauging stations (Liu and Gupta, 2007). Data assimilation (DA) has been traditionally used for uncertainty quantification and probabilistic forecasting in climate and ocean models. More recently, DA has also been applied in the field of hydrology to improve the accuracy of model predictions, assimilating variables such as soil moisture and streamflow (Gavahi et al., 2020; Hostache et al., 2020; Moradkhani et al., 2005; Xu et al., 2020), and has proved to be a powerful approach to real-time forecasting by updating the model state variables and parameters when new observations become available (Hostache et al., 2018; Moradkhani et al., 2019). The spatiotemporal resolution of remote sensing data is particularly appropriate for assimilation into large-scale hydrological and climate models (Abbaszadeh et al., 2018; Azimi et al., 2020; Lievens et al., 2017). On the other hand, observations at in situ gauging stations are still the most commonly used ones in hydrodynamic modelling (Jafarzadegan et al., 2021), with the inconvenience that such data are scarce in their distribution in terms of space. This is so because the spatial and temporal resolutions of satellite data are often too low to allow for their integration into high-resolution small-scale hydrodynamic models. Due to the rapid dynamics of some flood events in small and medium-scale catchments, it is not possible to work with a time resolution longer than one day, and, especially in flood extent analysis, with spatial resolutions much greater than the resolution of the numerical model itself. Since satellite products are still not always able to provide these temporal and spatial resolutions, the integration of these data into hydrodynamic models tends to be rather recent, and usually focused on large rivers (Brêda et al., 2019; Dasgupta et al., 2021a, 2021c; Meyer Oliveira et al., 2021; Wongchuig-Correa et al., 2020).

Most DA frameworks are based on the Kalman Filter and its variants (Annis et al., 2022; Jafarzadegan et al., 2021; Muñoz et al., 2022; Revilla-Romero et al., 2016; Wongchuig-Correa et al., 2020). These techniques do not require a very large number of model simulations,

* Corresponding author.
E-mail address: g.glores@udc.es (G. García-Alén).

https://doi.org/10.1016/j.jhydrol.2023.129667
Received 13 January 2023; Received in revised form 12 April 2023; Accepted 3 May 2023
Available online 16 May 2023

which is a clear advantage when applied to near-real-time forecasting. However, they assume a Gaussian distribution of model and observation errors which in general are not realistic in real-world data. Therefore, the capacity of Particle Filter (PF) methods to handle non-linear and non-Gaussian systems has attracted the attention of the research community in recent years (Van Leeuwen et al., 2019). Unfortunately, degeneracy affects PF methods, in that most of the particles are of very little weight after a few assimilation steps. This results in a large weight variance, and reduces the ability of the particle ensemble to assess uncertainty and to correctly approximate the posterior distribution of the model parameters. The Tempered Particle Filter (TPF) (Herbst y Schorfheide, 2019) is one approach that was developed to deal with such limitations. TPF reduces degeneracy based on a factorization of the likelihood using tempering coefficients that iteratively inflate the posterior probability variance. Such an approach has already been used for DA into flood models (Di Mauro et al., 2022; Di Mauro et al., 2021).

Previous studies focusing on DA into hydrodynamic models assimilate flood extent maps (Dasgupta et al., 2021a; Dasgupta et al., 2021b), altimetry (Brêda et al., 2019), water stage (Giustarini et al., 2011; Matgen et al., 2010; Oubanas et al., 2018) or discharge and water stage jointly (Jafarzadegan et al., 2021). In the present study we extend the TPF framework to the joint assimilation of soil moisture data from the Soil Moisture Active Passive (SMAP) satellite and streamflow data from a gauging station. The joint assimilation of soil moisture and streamflow through particle filter-based methods has already shown its effectiveness in large-scale hydrological models, for instance in the work of Yan and Moradkhani (2016), where a distributed hydrological model of a 7400 km^2 basin was used, yet it has never been applied to a small-scale hydrological-hydrodynamic model based on two-dimensional shallow water equations (2D-SWE).

The Landro basin (199 km^2) in north-western Spain was used as a case study. Numerical modelling was carried out using Iber+ (García-Feal et al., 2018), a GPU parallelized version of the Iber software (Bladé et al., 2014) that solves the 2D-SWE including rainfall-runoff transformation processes (Cea and Bladé, 2015). Twelve storm events of 48-hours were analysed. First, a sensitivity analysis (SA) was performed to identify the parameters with the highest impact on the model output. The TPF was then applied to each event independently in order to find sets of feasible parameters. The assimilation process started from a random set of particles, and a common standard deviation was assumed for all the parameters Based on the obtained parameter sets, we conducted a regression analysis to investigate how the prior information of each event (antecedent rainfall, soil moisture and streamflow) relates to the model parameters. Finally, the TPF was again applied to each of the twelve events using a first guess (i.e., a first set of particles) with parameter sets derived from the prior information (antecedent rainfall, soil moisture and streamflow) for each event.

2. Methodology

2.1. Numerical model

The numerical model used in this study is the freely distributed software Iber+ (García-Feal et al., 2018), which solves the 2D-SWE by using GPU parallelization techniques. The mass and momentum conservation equations solved by the model can be expressed as:

$$\frac{\partial h}{\partial t} + \frac{\partial q_x}{\partial x} + \frac{\partial q_y}{\partial y} = R - f \tag{1}$$

$$\frac{\partial q_x}{\partial t} + \frac{\partial}{\partial x}\left(\frac{q_x^2}{h} + g\frac{h^2}{2}\right) + \frac{\partial}{\partial y}\left(\frac{q_x q_y}{h}\right) = -gh\frac{\partial z_b}{\partial x} - gh\frac{n^2}{h^{10/3}}|q|q_x \tag{2}$$

$$\frac{\partial q_y}{\partial t} + \frac{\partial}{\partial x}\left(\frac{q_x q_y}{h}\right) + \frac{\partial}{\partial y}\left(\frac{q_y^2}{h} + g\frac{h^2}{2}\right) = -gh\frac{\partial z_b}{\partial y} - gh\frac{n^2}{h^{10/3}}|q|q_y \tag{3}$$

where h is the water depth, q_x, q_y and |q| are the two components of the unit discharge and its modulus, z_b is the bed elevation, n is the Manning's coefficient, g is the gravity acceleration, R is the rainfall intensity, and f is the infiltration rate. These equations are solved using an unstructured finite volume solver that includes a specific numerical scheme for hydrological applications (Cea and Bladé, 2015). As shown in several recent studies, the 2D-SWE can be used to model rainfall-runoff transformation and surface runoff with a relatively high resolution at spatial scales ranging from hillslopes to small and medium-size catchments (Cea et al., 2016; Cea et al., 2010; Cea and Bladé, 2015; Costabile and Costanzo, 2021; Ferraro et al., 2020; Fraga et al., 2019; García-Alén et al., 2022; Sanz-Ramos et al., 2021; Uber et al., 2021).

Iber + includes several formulations to compute infiltration losses. In the current study, the physically-based Green-Ampt formulation was used (Chow et al., 1988). In its implementation in Iber+, the infiltration rate is estimated as:

$$f_{pot} = k_s\left(1 + \frac{(h+\psi)}{b}\right) f = \min\left(f_{pot}, \frac{h}{\Delta t}\right) \tag{4}$$

where f_{pot} is the potential infiltration rate, k_s is the saturated soil permeability in the vertical direction, h is the water depth over the terrain, ψ is the suction in the unsaturated soil layer, b is the thickness of the saturated soil layer, and Δt is the computational time step. The real infiltration rate (f) is limited by the availability of water over the terrain (h). The suction (ψ) and the saturated permeability (k_s) are model parameters to be defined by the user, while the thickness of the saturated soil layer (b) is updated as the total infiltration depth increases, thus:

$$b = b_0 + \frac{F}{\phi} F = \int_0^t f dt \tag{5}$$

where b_0 is the initial thickness of the saturated soil layer, ϕ is the porosity of the soil, and F is the total infiltration depth. *Since Iber + is a 2D model in which the flow in the vertical direction is not resolved, the average moisture content of the soil layer (θ) is computed from the thickness of the saturated layer (b) as:*

$$\theta = \frac{b}{d_s}\phi \tag{6}$$

where d_s is the total thickness of the soil layer; the total thickness of the soil layer (d_s) and its porosity (ϕ) are parameters to be defined by the user. In Iber+, the initial thickness of the saturated soil (b_0) is defined by the user through the initial degree of saturation ($S_{r,0}$) of the soil. Given Equation (6) and the relationship between soil moisture, degree of saturation and porosity of the soil ($\theta = S_r\phi$), b_0 is estimated according to:

$$b_0 = S_{r,0} d_s \tag{7}$$

In addition to infiltration, the model considers initial losses (I_a) that can be satisfied by the initial rainfall or by the available overland water depth.

2.2. Sensitivity analysis

A global sensitivity analysis (SA) of the model output to the infiltration parameters was performed in order to identify the most relevant parameters to be included in the data assimilation. The five parameters analysed were: saturated soil permeability (k_s), Manning's roughness coefficient (n), soil suction (ψ), soil initial saturation ($S_{r,0}$), and initial losses (I_a). All the parameters were considered to be homogeneous in space except the bed roughness coefficient, whose spatial distribution was predefined based on the spatial distribution of land uses in the basin. Thus, the sensitivity to this parameter was assessed by considering a multiplier that was applied to scale its predefined spatial distribution. Regarding the porosity and soil layer parameters, these were not taken into account in the SA since, as described in section 3.3 below,

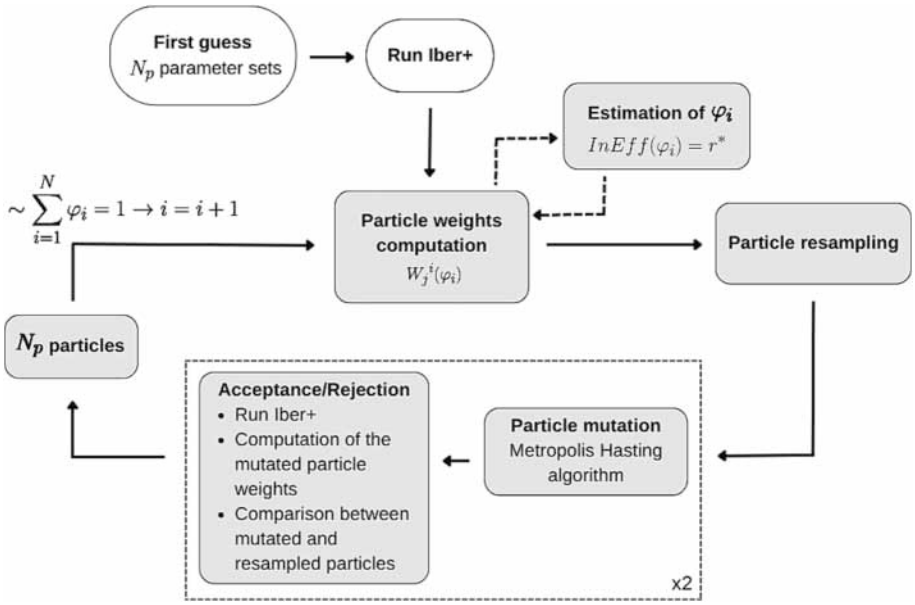

Fig. 1. Flow chart of the data assimilation framework. *Np* is the number of particles, φ_i is the tempering factor at the i th iteration, N is the number of iterations, $InEff(\varphi_i)$ is the ensemble inefficiency ratio, r^* is a target value, and $W_j^i(\varphi_i)$ is the global weight of the j^{th} particle in thei^{th} iteration.

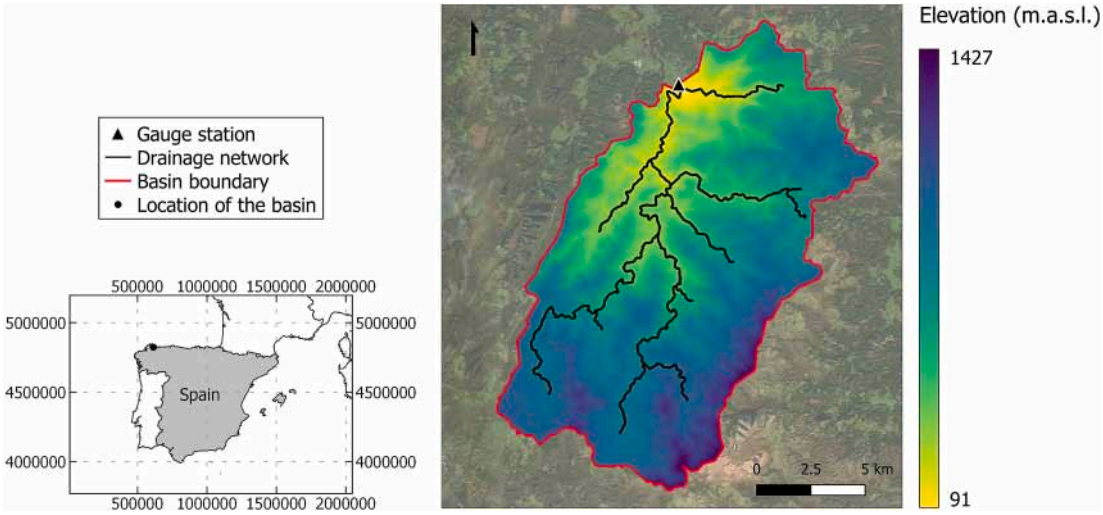

Fig. 2. Landro basin.

both were fixed for all simulations.

5000 parameter sets were randomly generated using the Latin Hypercube Sampling (LHS) within a predefined plausible range of variation for each parameter. The numerical model was run with each parameter set in a representative sample of 5 storm events. The outlet hydrograph obtained with each parameter set was compared to a synthetic reference hydrograph, using the Mean Absolute Difference (MAD) to quantify the degree of dissimilarity between hydrographs. The synthetic reference hydrograph was obtained by running the model with the mean value of the range of variation of each parameter. The MAD of all computations was analysed using the moment-independent importance measure (δ) proposed by Borgonovo (2007), as well as the first-order variance-based sensitivity indices ($S1_i$), in order to quantify the effect of each parameter on the outlet hydrograph. Although variance-based importance measure indices are often used, they rely on the assumption that the variance is sufficient to describe output variability (Saltelli, 2002). By contrast, moment-independent importance measures analyse the effect of the parameters without relying uniquely on the output variance.

2.3. Joint assimilation of soil moisture and discharge data

Particle Filter (PF) methods follow a two-step iterative procedure that includes predictions (model forward simulations) and analysis (updating particle probabilities and/or state variables by optimally combining the simulation results and the observations). The prior and posterior probability distributions, which characterise model states before and after the assimilation, are approximated by a set of particles. In our case, each particle is a model simulation with its own set of parameters and associated state variables. PF methods are likely to degenerate unless the number of particles is very large, increasing exponentially with the dimension of the system state. Degeneracy leads to a high probability assigned to a very limited number of particles and negligible weights to all other particles (Van Leeuwen et al., 2019). Given that degeneracy issues have been noted in previous studies (Di Mauro et al., 2021), and also considering that a large number of particles implies a significant increase in the computational cost of DA, for the present study we used a variant of the PF, the so-called Tempered

Table 1
Main characteristics of the 12 rainfall events analysed.

Event number	Starting date	Total rainfall depth (mm)	Q_{peak} (m^3/s)	Runoff depth (mm)	Initial soil moisture from SMAP[1]
1	22/11/19	63	94.2	60	0.37
2	18/12/19	65	76.8	54	0.40
3	11/08/20	56	27.9	17	0.20
4	01/10/20	64	33.9	26	0.25
5	24/10/20	54	53.8	24	0.29
6	10/12/20	25	43.9	13	0.38
7	30/12/20	41	40.1	23	0.40
8	24/01/21	40	87.2	30	0.40
9	02/02/21	34	49.7	16	0.40
10	11/02/21	59	72.7	52	0.40
11	17/06/21	69	44.1	25	0.29
12	02/10/21	47	29.1	9	0.23

[1] Two hours before the start of the event and averaged over the whole basin.

Table 2
Hydrological parameters considered in the study, and their range of variation.

Parameter	Range of variation in DA
k_s(mm/h)	0.3 – 10
Manning multiplier (-)	0.5 – 5
ψ(mm)	55 – 355
$S_{r,0}$(-)	0.2 – 1
I_a(mm)	0 – 30

Particle Filter (TPF) method (Herbst y Schorfheide, 2019). This relatively novel approach applies tempering coefficients to inflate the likelihood within an iterative process, respecting the Bayes' formula.

The Bayes theorem in a PF can be formalised as follows:

$$p(m|o) = \frac{p(o|m)}{p(o)} p(m) \tag{8}$$

where $p(m|o)$ is the conditional probability of the model given the observation, also called posterior or analysis, $p(m)$ is the probability of the model, also called prior or background, $p(o|m)$ is the conditional probability of the observation given the model, also called the likelihood of the observations, and $p(o)$ is a normalisation factor.

In the TPF, the likelihood $p(o|m)$ in Equation (8) is factorised as:

$$p(m|o) = \frac{\prod_{i=1}^{N} (p(o|m)^{\varphi_i})}{p(o)} p(m), with \sum_{i=1}^{N} \varphi_i = 1 \tag{9}$$

where φ_i is the tempering factor at the i^{th} iteration, this small enough to enable a substantial likelihood variance inflation, and N is the number of iterations. The tempering coefficients must add up to one in order to follow the Bayes formula (Equation (8). This factorisation enables the decomposition of the assimilation into several tempering steps, where the degeneration problem is overcome by the inflation of the likelihood variance.

Following the PF formulation, and assuming as independent both the observations assimilated into this study (soil moisture and discharge), $p(m|o)$ can be estimated at each tempering iteration i, thus:

$$\begin{aligned} p_i(m|o) &\approx \sum_{j=1}^{Np} W_j^i(\varphi_i)\delta(m - m_j) W_j^i(\varphi_i) \\ &= \frac{\prod_{i=1}^{Ni} (p_Q(o|m_j)^{\varphi_i})}{p_Q(o)} \frac{\prod_{i=1}^{Ni} (p_\theta(o|m_j)^{\varphi_i})}{p_\theta(o)} \end{aligned} \tag{10}$$

where W_j^i is the global weight of the j^{th} particle in the i^{th} iteration, δ is the Dirac delta function, Np is the number of particles, m_j is an ensemble of size Np model states, Ni is the number of iterations up to the i^{th} iteration; $p_Q(o|m_j)$ and $p_\theta(o|m_j)$ are the conditional probabilities of the observed discharge (Q) and soil moisture (θ) estimated given the j^{th} model state, and $p_Q(o)$ and $p_\theta(o)$ are the normalization factors of the observed discharge and soil moisture, respectively. Observation errors are assumed to be independent of each other.

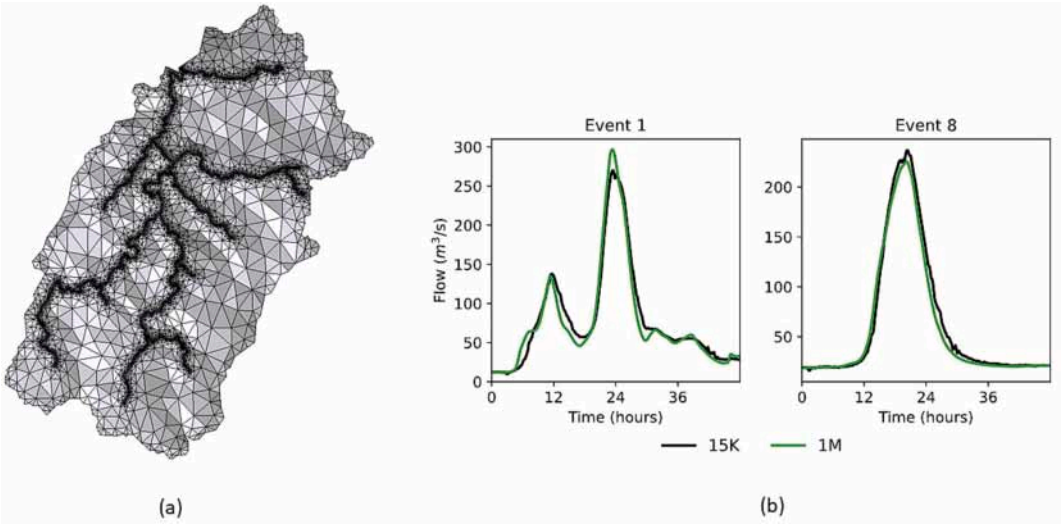

Fig. 3. (a) 15 K element mesh taken for the numerical simulation of the selected events in the Landro river basin; (b) Hydrographs obtained for event 1 (left) and 8 (right) using a mesh of 15 K elements (black) and 1 M elements (green). (For interpretation of the references to colour in this figure legend, the reader is referred to the web version of this article.)

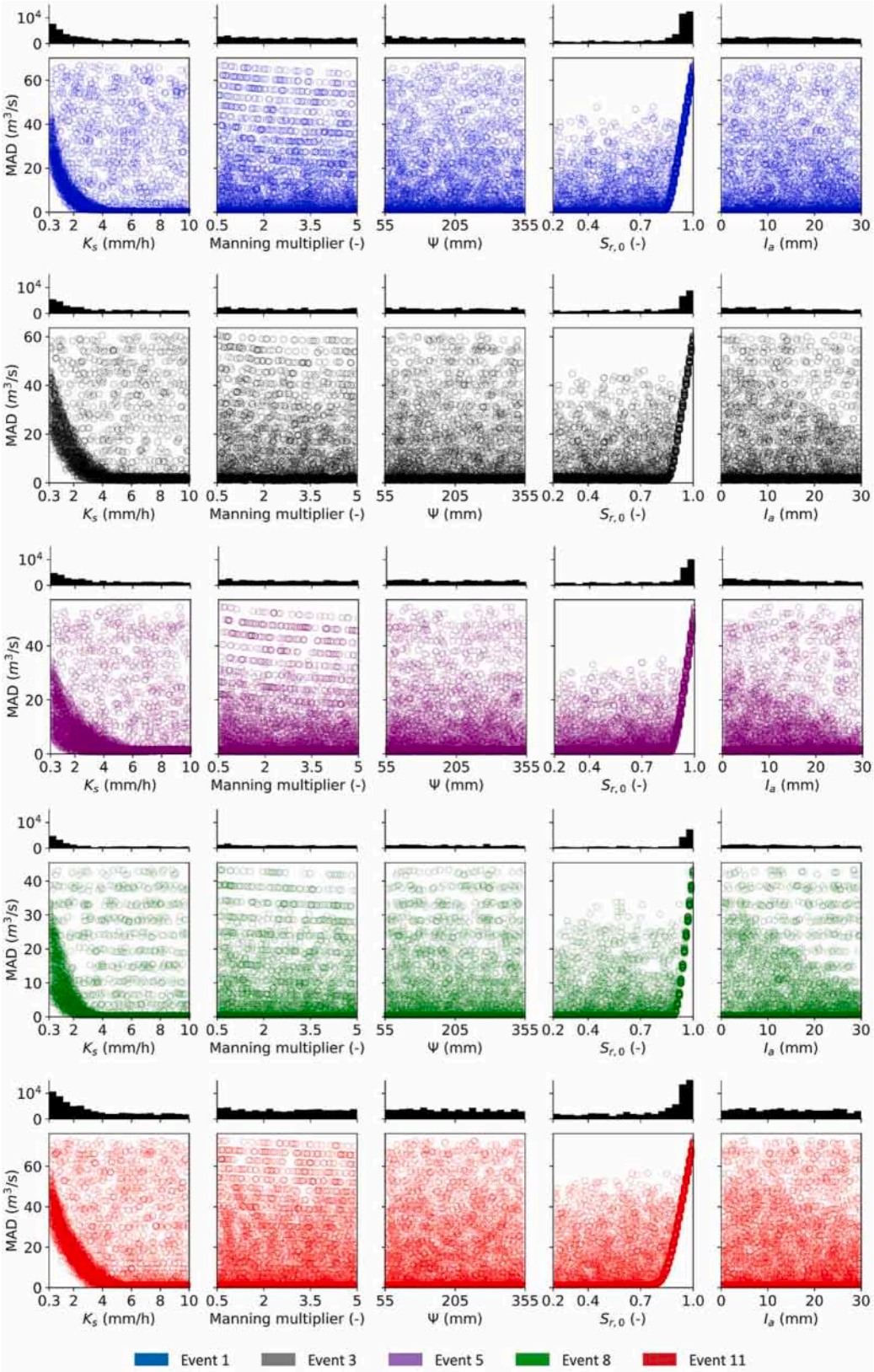

Fig. 4. Results of the global sensitivity analysis based on MAD.

A flow chart of the data assimilation framework is presented in Fig. 1. In the first iteration, an initial set of parameters (i.e., first guess) must be defined to create the first set of particles. After the model simulations, particle weights are estimated using the observations and the tempering factor (φ_i). This exponent ranges between 0 and 1 ($0 < \varphi_i < 1$) and makes it possible to retain a substantial number of particles with significant weights. It is increased at each iteration and represents the solution to the ensemble inefficiency ratio ($InEff(\varphi_i)$):

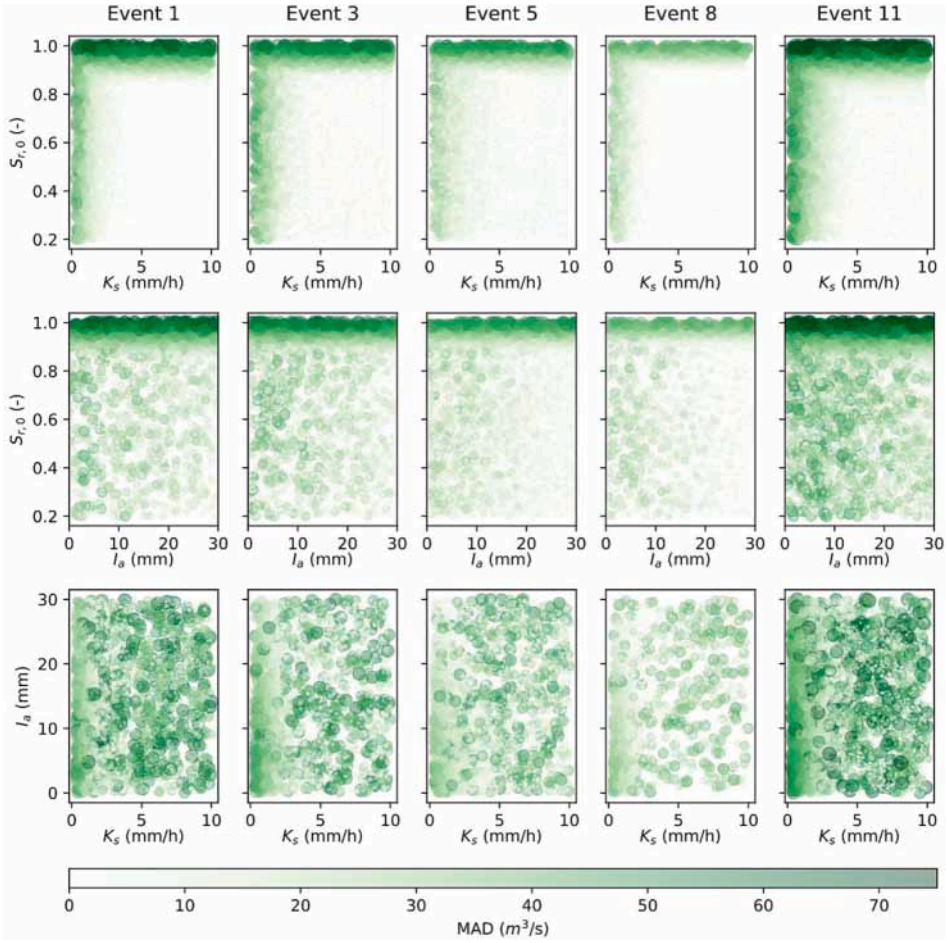

Fig. 5. Interactions over the most sensitive model parameters: k_s, $S_{r,0}$ and I_a. Each dot represents the result of a simulation, the size and colour of the dot being proportional to the resulting MAD value.

$$InEff(\varphi_i) = r^*, withInEff(\varphi_i) = \frac{1}{Np}\sum_{j=1}^{Np}\left(W_j{}^i(\varphi_i)\right)^2 \quad (11)$$

where a targeted inefficient ratio (r^*) is previously defined.

The particles with high weights are resampled after each iteration i using a Sequential Importance Resampling (SIR). Particles are replicated proportionally with their weights: those with an associated low importance weight are replaced with replicas of those having higher weight. Particles are equally weighted after resampling. Next, two mutations are applied to the particles (model parameters are slightly perturbed). These mutations, based on a Metropolis Hasting (MH) algorithm, allow the ensemble to regain diversity after each resampling step. The mutated particle simulations are carried out, and the mutated particles are accepted or rejected based on their likelihood as compared to the resampled particles likelihood. After two runs of MH, a new iteration is started with the estimation of a new tempering coefficient (φ_i) and the computation of the particle weights. The entire process is repeated until the sum of the tempering coefficients is equal to unity, i. e. iterations are ended when $\varphi_N = 1 - \sum_i^{N-1}\varphi_i$, where N is the total number of iterations. Detailed descriptions of the TPF can be found in Di Mauro et al, 2022, and Herbst and Schorfheide, 2019.

The TPF approach was applied twice: (1) using as first guess a set of random particles from the ranges of variation, and assuming in the mutation of the particles a standard deviation common for all parameters; (2) using a relationship between model parameters and basin antecedent conditions to establish the initial set of particles (first guess) and to define the standard deviation of each parameter. In both cases the number of particles (Np) used was equal to 15 and a targeted inefficient ratio (r^*) equal to 2 was assumed. For the comparison of the simulated and observed discharge, we used the Mean Absolute Error (MAE) normalised to the peak flow (%), the Nash Sutcliffe Efficiency (NSE), and the relative volume error over the hydrograph. For the comparison of soil moisture values, the RMSE was used.

3. Case study and model setup

3.1. Study area

The Landro basin is located in the north-western Iberian Peninsula (Fig. 2). A streamflow gauging station managed by the regional water administration (Augas de Galicia) is located near the basin outlet, receiving runoff from an area of 199 km^2. The altitude ranges from 91 to 1427 m above sea level, with an average terrain slope of 27%. The soil is made up of gneiss metasediment and granitic rock. Most of the basin is covered by eucalyptus, pine forests and scrublands, with only a very small proportion of cultivated areas in the main channel floodplains. Its location confers on the basin an Atlantic climate, marked by abundant rainfall throughout the year, with storms occurring mainly during the winter season. The mean annual rainfall depth is 1412 mm and the average annual maximum daily precipitation is 62 mm. The Landro river has a length of 42 km and follows a S-N direction. On average, the river has a minimum, mean and maximum annual streamflow equal to 1.44, 5.8 and 16.9 m^3/s, respectively.

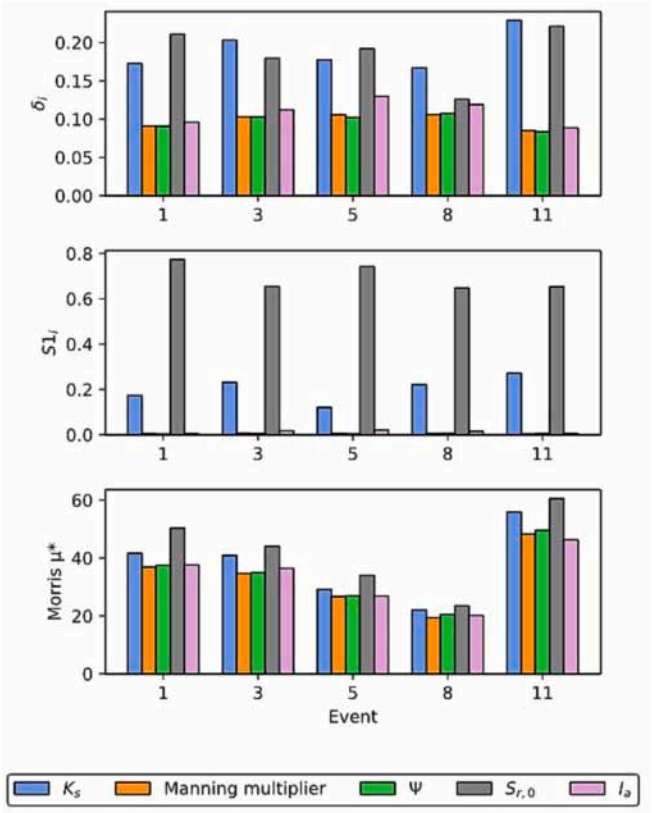

Fig. 6. Borgonovo moment-independent importance measure (top), first-order Sobol sensitivity indices (middle) and the Morris sensitivity measure μ* (bottom) for each model parameter.

3.2. Observed data

3.2.1. Rainfall

Rainfall data since 2019 were provided by the regional meteorological agency (Meteogalicia) in the form of raster rainfall fields. Those were estimated from the combination of rain gauge and meteorological radar observations using a conditional merging technique (Pettazzi and Salsón, 2012), which improves the characterisation of the spatial distribution of rainfall by combining the advantages of rain gauges (high accuracy of rainfall data at ground level) and radar (high space resolution of the observations). The meteorological radar operated by Meteogalicia has spatial and temporal resolutions of 250 m and 5 min, respectively, while the rain gauge data has a temporal resolution of 10 min. The observed rainfall intensity data were implemented in the numerical model as raster fields with a spatial resolution of 250 m and a temporal resolution of 1 h.

From the period with available rainfall data, 12 storm events representing different peak flow and initial soil moisture conditions were selected (Table 1). Each of the events analysed has a total duration of 48 h.

3.2.2. River discharge

Discharge data for the 12 storm events were available from a stream gauge operated by the regional water administration (Augas de Galicia). The data were obtained from water-level measurements performed every 10 min, converted to discharge values using previously-calibrated rating curves. The location of the Landro gauging station is shown in Fig. 2 (Longitude: 613,652 UTMX-29 T ED-89; Latitude: 4,830,448 UTMY-29 T ED-89). The data provided by Augas de Galicia underwent an internal validation process in which erroneous observations were discarded. However, the uncertainty of the data is not provided. Within the framework of this study, it was assumed that the observed discharge had a maximum relative error of 10%, which is an order of magnitude used in similar studies (Abbaszadeh et al., 2018).

3.2.3. Soil moisture

Soil moisture data were retrieved from the Soil Moisture Active

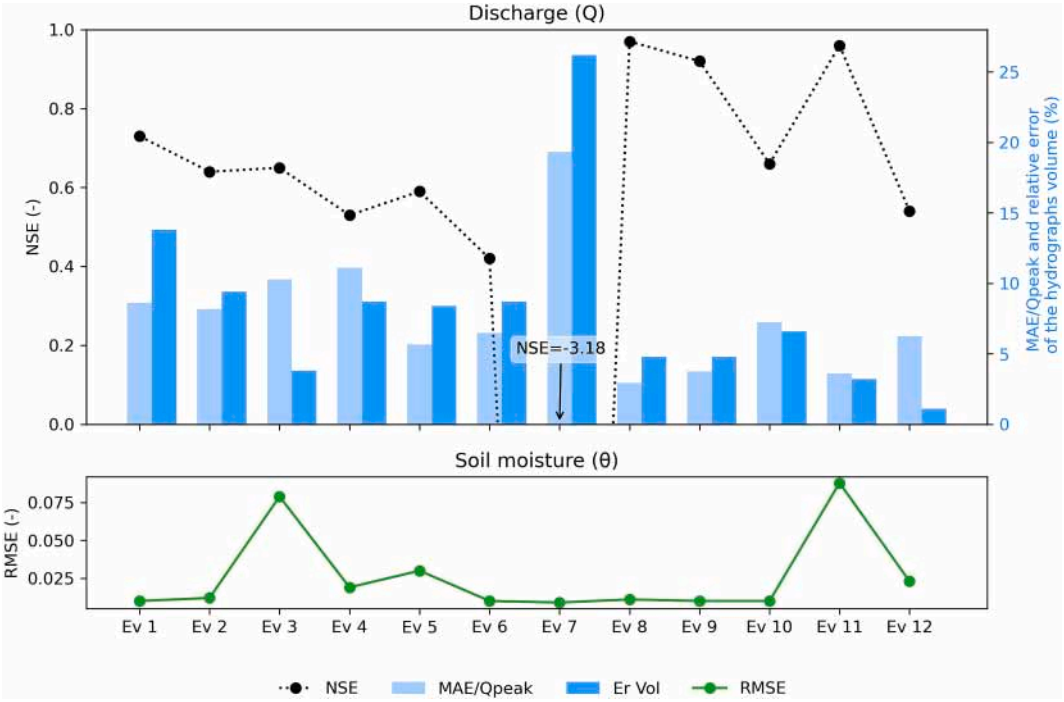

Fig. 7. Results obtained after the first application of the TPF approach. For each event, the adjustment achieved for the discharge (in terms of MAE/Qpeak, NSE, and relative error of the volume of the hydrographs) and soil moisture (in terms of RMSE) are indicated.

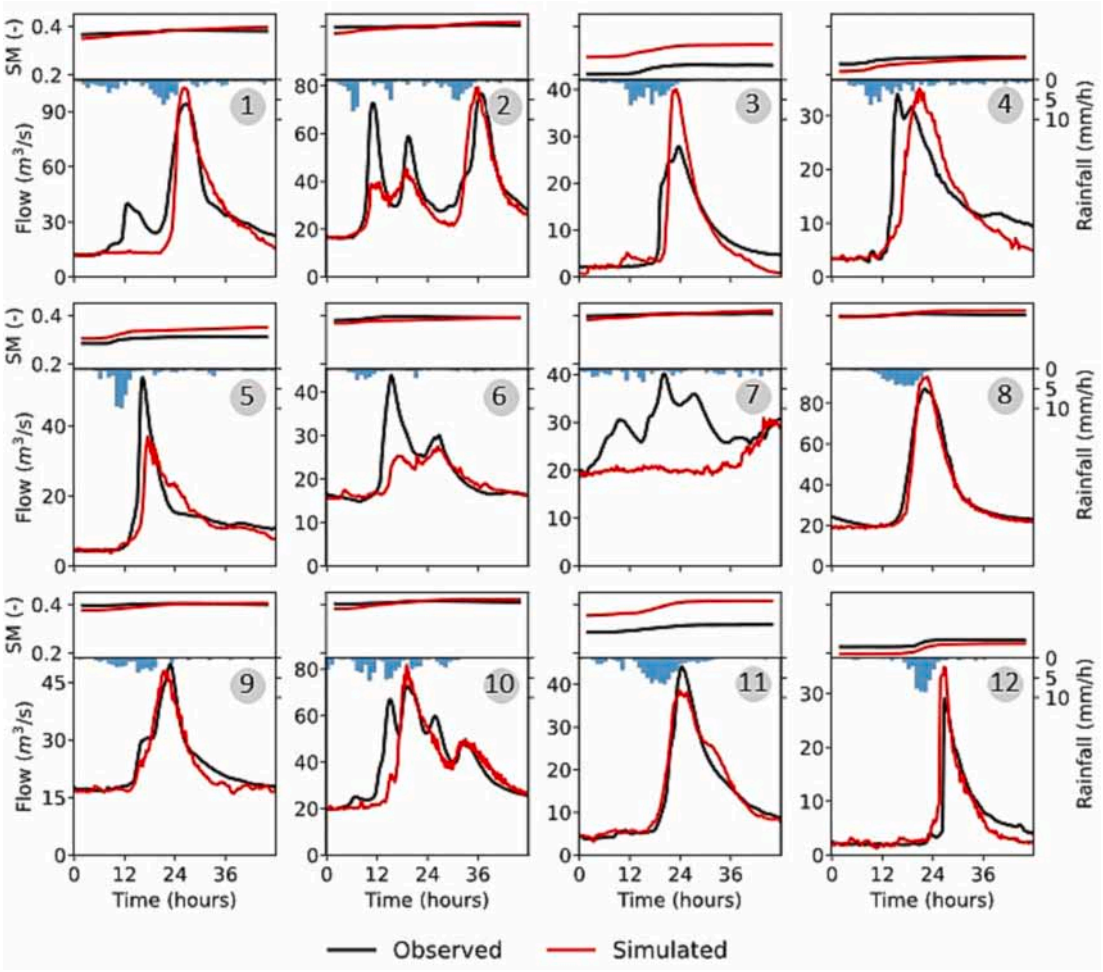

Fig. 8. Result of observed (black) and simulated (red) hydrographs after the joint assimilation of discharge and soil moisture in the first application of the TPF approach. (For interpretation of the references to colour in this figure legend, the reader is referred to the web version of this article.)

Passive (SMAP) satellite provided by the National Snow and Ice Data Center. Among the different products available there, the Root Zone Soil Moisture Analysis Update (SPL4SMAU) was used, which is obtained via the assimilation of SMAP L-band brightness temperature data into the Catchment land surface model using ensemble-based Kalman filtering (Reichle et al., 2020). The product (version 5) provides instantaneous soil moisture fields for both the surface (0–5 cm) and root zone (0–100 cm) layers at 3-h intervals over an Earth-fixed, global cylindrical 9-km Equal-Area Scalable Earth Grid (EASE-Grid 2.0) (Peng et al., 2021; Reichle et al., 2017). Due to the rapid dynamics of some flood events, the temporal resolution of satellite data is one of the main limitations of integrating satellite products into the numerical simulation of small-scale hydrodynamic models. The SPL4SMAU product has a temporal resolution that is well suited for its application in short-duration storm events.

In this study, the soil moisture value for the root zone was used, since it was considered the most representative means of characterising the infiltration capacity of the soil. In the assimilation of observed data, the average soil moisture in the whole catchment was used, with the SMAP data having an uncertainty value of 0.02 m^3/m^3 (Reichle et al., 2019). Table 1 indicates the soil moisture value at the beginning of each storm event.

3.3. Model setup

Whereas section 2.1 presented a general description of the numerical model and the selected infiltration model, here we will specify the particular characteristics of the numerical model of the Landro basin, including aspects such as the spatial discretisation used and the range of variation of the hydrological parameters considered.

In Iber+, the Digital Terrain Model (DTM) values are interpolated to the nodes of the computational mesh using a bilinear interpolation method. The elevation value at each mesh vertex is interpolated using 5 m spatial resolution LiDAR-derived DTM provided by the National Geological Institute of Spain (IGN-CNIG, 2021). Bottom friction is modelled in Iber + with the Manning's formula. For this study, the Manning's roughness coefficient was defined according to the land use map of the European project CORINE Land Cover 2018 (CLC2018) (European Union Copernicus Land Monitoring Service, 2018) and the recommendations of the Methodological Guide for the Development of the National Floodplain Mapping System (Sánchez and Lastra, 2011), which proposes a Manning's coefficient for each land use in CORINE. Since the roughness values required when computing the overland flow with the 2D-SWE are sometimes higher than those commonly used for riverbeds (Cea et al., 2016; Fraga et al., 2013; Sanz-Ramos et al., 2021), the Manning's coefficient multiplier was used here with a rather wide range of variation. Regarding the numerical simulation of the base flow, this was set constant for each storm event and was equal to the observed flow at the beginning of the corresponding event.

Rainfall losses were computed using the Green-Ampt infiltration model. We considered five parameters of this model (k_s, n, ψ, $S_{r,0}$, I_a), and chose a range of variation capable of representing a wide variety of soils (Table 2). The other two parameters contemplated in the implementation of this infiltration model were fixed in all simulations: total

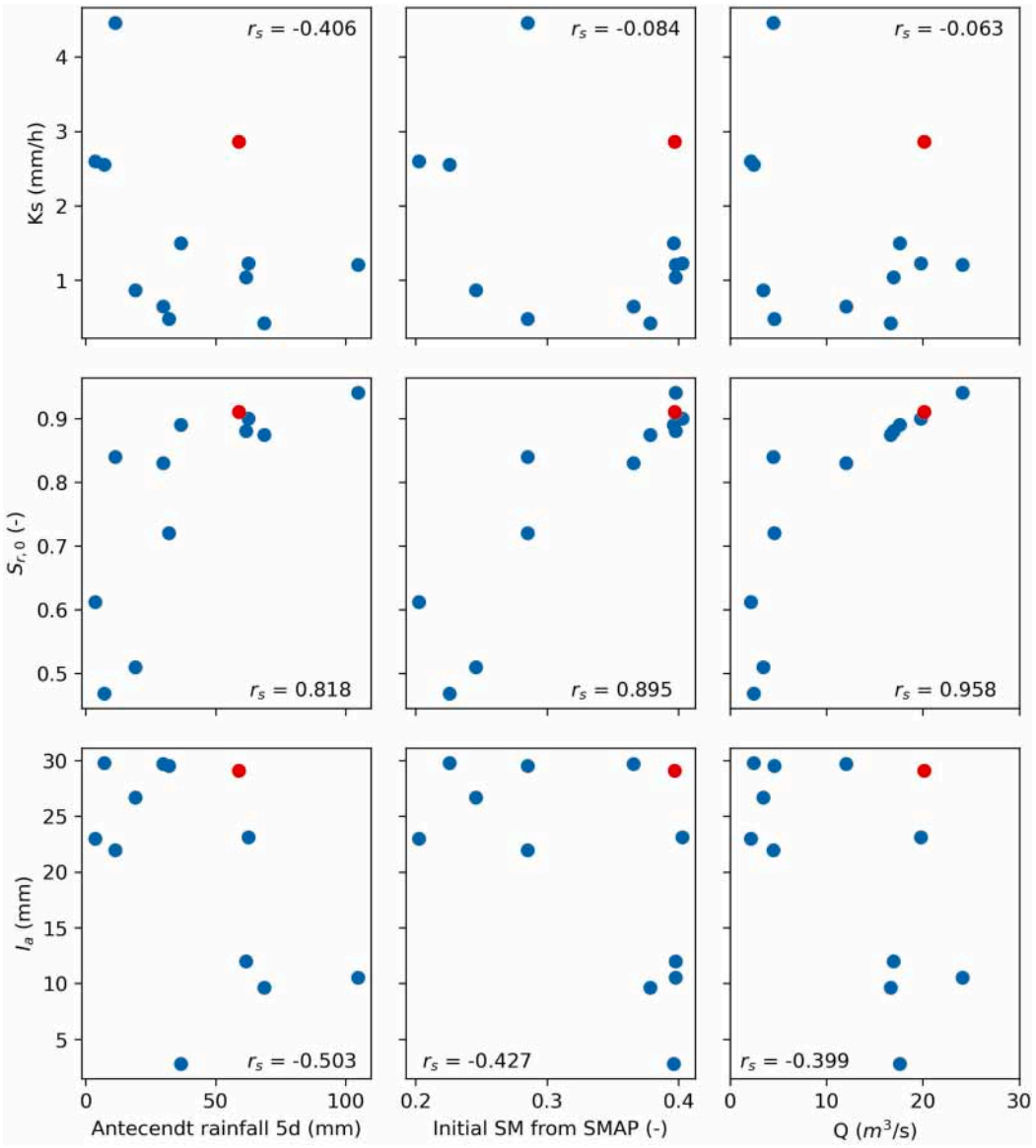

Fig. 9. Relationships between the numerical model parameters considered for the joint assimilation and the observed 5-day antecedent rainfall (left column), initial soil moisture observed by SMAP (middle column), and base flow at the beginning of the event (right column). Event 7, the only event in which negative NSE values were obtained, is represented in red. The Spearman's rank (r_s) correlation coefficient is indicated. (For interpretation of the references to colour in this figure legend, the reader is referred to the web version of this article.)

thickness of the soil layer (d_s), and porosity (ϕ). The total thickness of the soil layer (d_s) was set to 1 m to remain consistent with the SMAP-derived soil moisture data (see section 3.2.3). The porosity (ϕ) of the soil was set to 0.42, since it was considered to be a parameter directly related to soil type and with low variation from one event to another. This value was set within the range of variation shown in the study by Fraga et al. (2019) over the same area.

The computational domain was discretised with an unstructured non-uniform mesh, using a coarser mesh size in the hillslopes and a finer mesh size in the channel network. This is a common procedure in 2D-SWE models that allows for a reduction in computational cost without compromising the accuracy of the results (Costabile and Costanzo, 2021). In order to establish the mesh size that would be used in the numerical simulations, a mesh convergence analysis was performed, using events 1 and 8. The results with a mesh of 1 M elements were used as a reference. The resolution of this reference mesh is equal to 5 m on the watercourse and 25 m on the hillslopes. These resolutions are consistent with García-Alén et al. (2022), where it is concluded that higher mesh resolutions provide similar results in terms of the output hydrograph. The use of a 15 K element mesh, with a mesh resolution of 40 m in the water course and 800 m in the hillsides (Fig. 3a), made it possible to reduce the computational cost of the simulation by a factor of 90 times, and provides a MAD (Mean Absolute Difference) normalised to the peak flow lower than 3.5% in both events when compared with the reference simulation on a 1 M elements mesh (Fig. 3b). Thus, the 15 K mesh was taken for the numerical simulation of the selected events.

4. Results and discussion

4.1. Sensitivity analysis

The sensitivity analysis (SA) was based on five different events that were simulated using 5000 different parameter sets. Fig. 4 includes scatter plots that show the relationship between the model parameters and the MAD relative to the comparison of the simulated hydrographs with the hydrographs computed in the reference simulation. In this

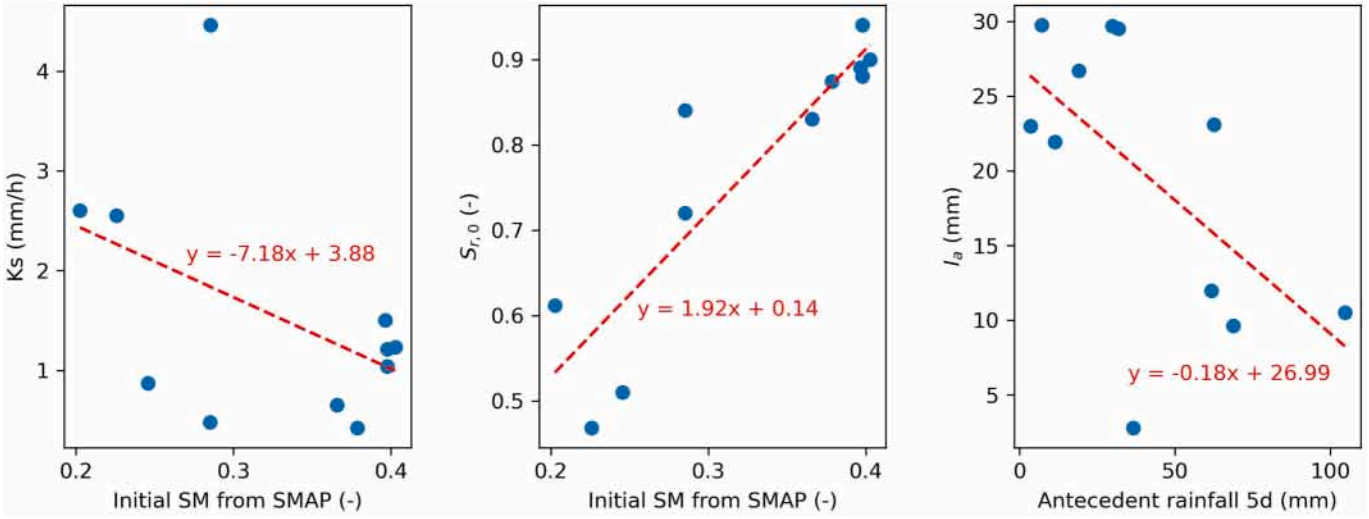

Fig. 10. Linear relationships between k_s and the initial SM form SMAP (left), $S_{r,0}$ and the initial SM from SMAP (centre), and I_a and the 5-day antecedent rainfall (right). Event 7 was excluded in the estimation of the linear regressions.

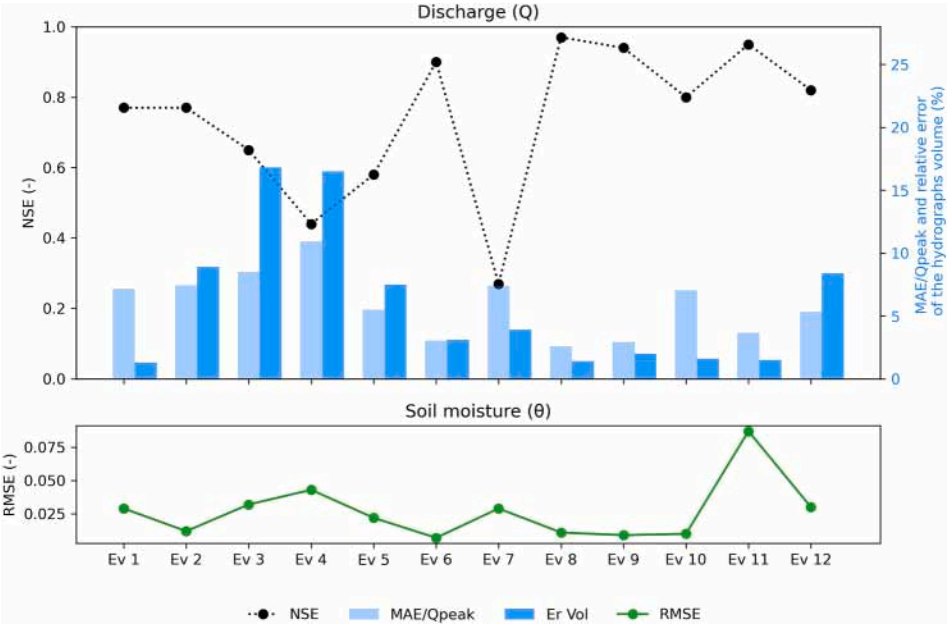

Fig. 11. Results obtained after the second application of the TPF approach. For each event, the adjustment achieved for the discharge (in terms of MAE/Qpeak, NSE, and relative error of the volume of the hydrographs) and soil moisture (in terms of RMSE) are indicated.

comparison the entire time series of the simulated hydrographs were considered. As mentioned in section 2.2, this reference simulation was obtained by running the model with the mean value of the range of variation of each parameter. In these plots, each point corresponds to a single simulation result using a given parameter set. A weighted histogram (weighted by the MAD of each simulation) is included above each scatter plot. Most of the samples providing high MAD values are grouped within a small range of k_s values. On the contrary, the outlet hydrograph does not seem to be sensitive to the Manning multiplier or to the suction parameter (ψ), since uniform histograms are observed for these two parameters in all the events. The initial degree of saturation ($S_{r,0}$) tends to be very relevant when it is close to 1, and far less relevant when it is smaller than 0.8. Finally, the uniformity of the histograms indicates that the model is not very sensitive to the initial loss parameter (I_a).

Fig. 5 shows the interactions according to these three parameters (k_s, $S_{r,0}$ and I_a). For each of the five events and for the three pairs of parameters (k_s-$S_{r,0}$, k_s-I_a and $S_{r,0}$-I_a), MAD values obtained in each simulation are plotted in the parameter space. The size and colour of the dots are proportional to the MAD value. In the first row in Fig. 5 ($S_{r,0}$ against k_s), it can be observed that for high values of $S_{r,0}$ (close to 1), the results are independent of the value of k_s. However, when $S_{r,0}$ is far from its upper limit, a significant interaction is observed for low values of k_s. There is not a clear interaction between I_a and the other two parameters, confirming that the sensitivity of the model to this parameter is low.

To further quantify the relevance of each model parameter, several sensitivity measures were computed based on the MAD results: (1) the Borgonovo moment-independent importance measure (δ_i), (2) the first-order Sobol sensitivity index ($S1_i$) and (3) the sensitivity measure μ* derived from the Morris analysis. Fig. 6 provides the δ_i (top), $S1_i$ (middle) and μ* (bottom) results obtained for the five parameters and for the five events considered in the SA. The Borgonovo importance measure indicates that the model is more sensitive to k_s and $S_{r,0}$ than to

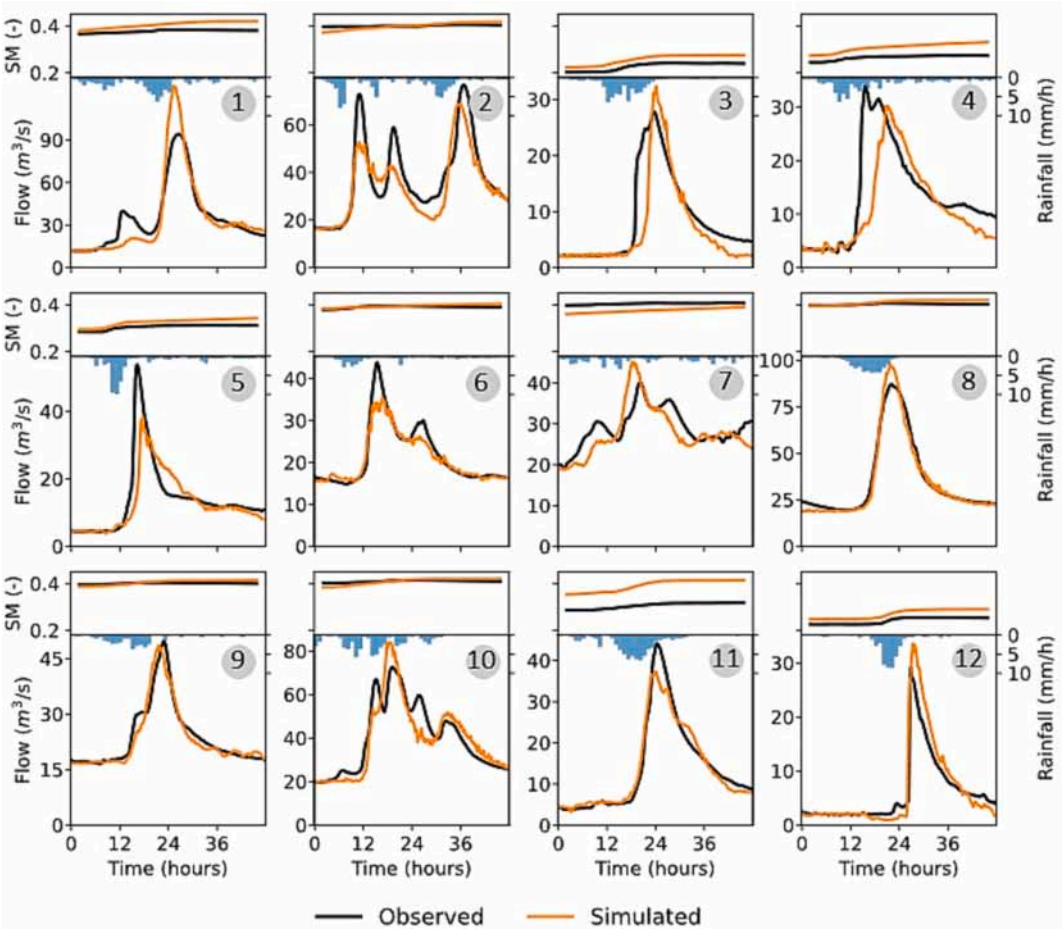

Fig. 12. Result of observed (black) and simulated (orange) hydrographs after the joint assimilation of discharge and soil moisture in the second application of the TPF approach. (For interpretation of the references to colour in this figure legend, the reader is referred to the web version of this article.)

the other 3 parameters. This result is consistent with the μ* values obtained in the Morris analysis, where the values of k_s and $S_{r,0}$ stand out slightly above the rest of the parameters. Regarding the Sobol's indices, the sums of the first-order indices are greater than 0.89 in all events, indicating a weak interaction among the parameters. Moreover, it can be deduced that the initial degree of saturation ($S_{r,0}$) is able to explain between 65% and 77% of the first-order MAD variance. Conversely, and although the effect of the initial losses (I_a) is already low, the Manning's coefficient multiplier and the suction (ψ) have a limited effect on the MAD. The effect of k_s is moderate in this case, with an average value of 0.13. Based on these results, it can be concluded that k_s, $S_{r,0}$ and, to a lesser extent, I_a, are the most relevant model parameters.

4.2. Joint assimilation of soil moisture and discharge data

Based on the SA results, the number of parameters considered in the DA was reduced to saturated soil permeability (k_s), initial degree of saturation ($S_{r,0}$) and initial losses (I_a). The range of variation considered for these parameters is shown in Table 2. The Manning's coefficient multiplier and suction were set to 4.5 and 136.5 mm in all the simulations. Thus, the chosen roughness coefficients maintain the same order of magnitude as in other overland flow studies where it has been observed that these coefficients tend to be higher than the ones commonly used in the simulation of river flows (Nguyen et al., 2016). The suction value was established from the literature, as based on previous experiences (see e.g., Chow et al., 1988).

As mentioned in section 2.3, 15 particles were considered in the Tempered Particle Filter (TPF) approach. Each particle corresponds to a model simulation with its own set of parameters and associated state variables. After the iterative process, 15 different outputs of streamflow and soil moisture were obtained. The ensemble expectation (average value of the 15 particles) was used to compare with observations and to evaluate the performance of the DA approach. In the first iteration of the assimilation (first guess), the parameter values of each particle were randomly selected from their range of variation. Also, in the application of the MH algorithm for the mutation of the particles carried out at each tempering iteration, a standard deviation equal to 1 was assumed for all parameters (1 (-) for $S_{r,0}$, 1 mm/h for k_s and 1 mm for I_a).

Fig. 7 summarises the performance metrics obtained for each event, while Fig. 8 shows the observed and simulated hydrographs and SM values. The agreement between modelled and observed hydrographs is good in most of the events, except in events 6 and 7. In both of these, and especially in event 7, the model was unable to reproduce the observed hydrograph. Considering the time variability of the observed rainfall in both events, the proposed methodology seems to be less effective in storm events with continuous and low-intensity rainfall that generates less pronounced peak discharges. Excluding the result of these events, the mean NSE value obtained for the other 10 events was 0.72. In general, a better fit was observed in the events with a well-defined isolated peak discharge (e. g., events 8, 9 and 11, with NSE values equal to 0.97, 0.92 and 0.96, respectively).

Concerning soil moisture, the RMSE between the simulations and observations was less than 0.02 in 8 of the 12 events, which can be considered very satisfactory. Events 3 and 11 both had poor performances, with RMSE values of 0.08 and 0.09, respectively.

In order to carry out this joint assimilation by reducing as much as

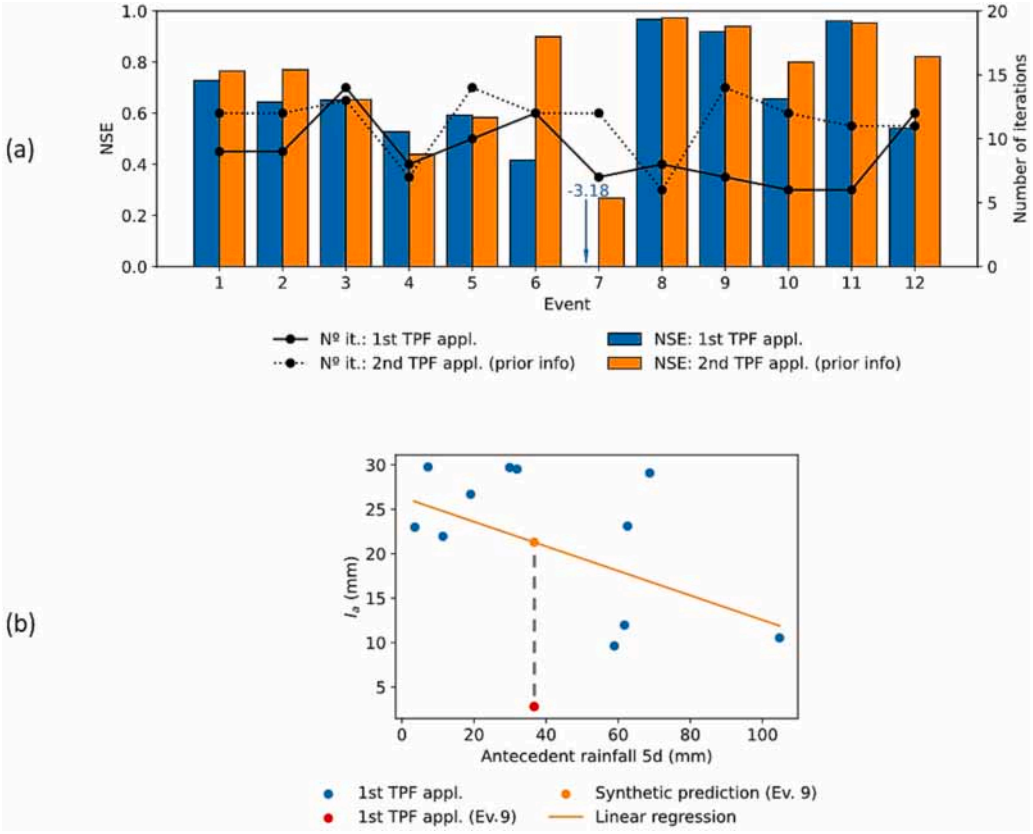

Fig. 13. (a) Results of NSE and number of iterations of the DA from the first (standard) and second (improved) application of the TPF approach. (b) Relationship between observed antecedent rainfall and the initial loss parameter achieved in the first (standard) application of the TPF approach; in red the result obtained for event 9, in orange the linear regression and the synthetic prediction from the antecedent rainfall observed in event 9. (For interpretation of the references to colour in this figure legend, the reader is referred to the web version of this article.)

possible the ranges of variation of the numerical parameters considered, we also searched for relationships between the parameters considered in the DA and the antecedent rainfall, soil moisture and streamflow of the basin. Fig. 9 shows the relationships obtained between saturated soil permeability (k_s), initial soil saturation ($S_{r,0}$) and initial losses (I_a), and also the following antecedent conditions of the basin: accumulated 5-day antecedent rainfall, initial moisture observed by SMAP, and base flow at the beginning of the event. The accumulated antecedent rainfall was estimated over the 5 days prior to the start of the event, in that it is a time period commonly used to estimate the antecedent moisture conditions of a basin (Brocca et al., 2008). Event 7, the worst in terms of NSE, is represented in red.

The saturated soil permeability does not show a clear trend with the antecedent conditions, with rather low Spearman's correlation coefficients (Fig. 8). Conversely, the initial SM exhibits a significant trend with the 3 antecedent conditions considered. The Spearman's rank correlation with the initial baseflow reaches 0.958, which is particularly high. A high correlation coefficient with the initial SM derived from SMAP is also observed. Regarding the initial losses, there is no evident relationship with the basin antecedent conditions. Although the Spearman's correlation coefficients are not high, these relationships could be used to at least reduce the parameter variance and thus optimise the number of iterations needed in the PF approach. Particularly for dry antecedent conditions, as seen in the results of I_a obtained for initial SM lower than 0.3 or base flow lower than 10 m3/s, it can be observed that I_a varies in a range between 20 and 30 m3/s.

4.3. Joint assimilation of soil moisture and discharge data using a first guess and parameter variances derived from prior information

The relationships between model parameters and antecedent conditions shown in Fig. 9 were used in a slightly different implementation of the TPF. Hence, those relationships were used: 1) to define the parameter standard deviations used in the particle mutations and; 2) to establish a set of parameters (synthetic prediction) derived from the basin antecedent conditions of each event. The synthetic parameter sets were utilised, together with the parameter standard deviations, to generate the first set of particles (first guess) of the assimilation.

A linear relationship was assumed for the three model parameters: between k_s and the initial SM from SMAP, $S_{r,0}$ and the initial SM from SMAP, and I_a and the 5-day antecedent rainfall (Fig. 10). In the estimation of the linear regressions, event 7 was not included due to its poor performance. The Pearson's coefficient values obtained for the relationships of k_s, $S_{r,0}$ and I_a were −0.46, 0.90 and −0.59, respectively. From the linear regressions, standard deviations of 0.074 (-) for $S_{r,0}$, 1.078 mm/h for k_s, and 7.159 mm for I_a were estimated.

Fig. 11 and Fig. 12 show the performance metrics obtained for each event, as well as the comparison between the observed and simulated hydrographs and SM. The results with this implementation of the TPF improve with respect to those obtained using the standard implementation, especially in terms of discharge, since in this case only 4 events gave a NSE lower than 0.7. The worst NSE was again on event 7, with a value of 0.27. However, the MAE normalised to the peak flow and the relative volume error over the hydrograph for this event indicate that the prediction was in agreement with the results observed. In terms of SM, no significant improvement was observed with respect to the standard implementation of the TPF. However, 9 of the 12 events remained with RMSE values in the range of 0.02–0.03, a result very close to the uncertainty value considered in the DA process (0.02). In event 11 a poor reproduction of the SM observations was obtained (RMSE equal to 0.087). Although the $S_{r,0}$ dis not match the observed SM from SMAP, and therefore the first guess was not adequate, the assimilation method was able to adapt to this outlier and eventually took it as a feasible parameter.

Fig. 13a shows the NSE obtained in the standard (blue) and improved (orange) applications of the TPF approach. After the implementation of

the prior information, the NSE always increased, except in event 4. Considering the 12 events, the average NSE was 0.37 in the first assimilation and increased to 0.74 after the implementation of prior information. If event 7 is excluded in the estimation of these average values, the mean NSEs obtained in the first and second implementations were 0.69 and 0.78, respectively. Fig. 13a also includes the number of iterations needed in the DA process, a value that is directly related to the number of model runs required and thus to the computational cost of the method. In general, an equivalent or even higher number of iterations was needed when the prior information was included. This increase in the number of iterations is in some cases related to outliers in the linear relationship between model parameters and antecedent conditions (Fig. 10), especially in the case of I_a and k_s, where the relation is less evident. For example, in the case of event 9 the value of I_a taken from the linear regression, and based on the 5-day antecedent rainfall (red dot in Fig. 13b), is very different from the value which yielded a good reproduction of the observed discharge data.

5. Conclusions

A particle filer-based data assimilation methodology to assimilate in situ observed discharge and satellite-derived soil moisture was proposed and applied to a 2D hydrological model based on the 2D-SWE. The proposed approach was based on the joint assimilation of soil moisture data provided by the SMAP satellite and discharge data measured at a gauging station. Twelve storm events registered in the Landro river basin (199 km^2) were analysed, and used to evaluate the effectiveness of the method.

This joint assimilation framework allowed for a correct reproduction of the basin outflow, with soil moisture values close to the observations for most storm events. A mean NSE value of 0.74 was reached for all twelve events. The results were in general more accurate in rainfall events that produced isolated peak flows. It was found that it was possible to relate some of the model parameters to the hydrological antecedent conditions of the catchment, in this way improving the assimilation process. The most significant correlation (Pearson's coefficient of 0.90) was identified with the initial soil saturation. The application of these relationships to the DA process lead to better performances, but was not always accompanied by a reduction in computational cost. The results of this case study, then, show that by considering only three hydrological parameters in the assimilation process, a good compromise between DA effort and model performance can be achieved.

Declaration of Competing Interest

The authors declare that they have no known competing financial interests or personal relationships that could have appeared to influence the work reported in this paper.

Data availability

No data was used for the research described in the article.

Acknowledgments

The authors acknowledge the support of Augas de Galicia and the Galicia Meteorological Agency (Metogalicia). Gonzalo García-Alén acknowledge the support of the INDITEX-UDC 2021 and 2022 Predoctoral Grants. The research reported herein was funded by the Luxembourg National Research Fund through the CASCADE (grant no. C17/SR/11682050) Project. Funding for open access charge: Universidade da Coruña/CISUG.

References

Abbaszadeh, P., Moradkhani, H., Yan, H., 2018. Enhancing hydrologic data assimilation by evolutionary particle filter and Markov chain Monte Carlo. Adv. Water Resour. 111, 192–204. https://doi.org/10.1016/j.advwatres.2017.11.011.

Annis, A., Nardi, F., Castelli, F., 2022. Simultaneous assimilation of water levels from river gauges and satellite flood maps for near-real-time flood mapping. Hydrol. Earth Syst. Sci. 26, 1019–1041. https://doi.org/10.5194/hess-26-1019-2022.

Azimi, S., Dariane, A.B., Modanesi, S., Bauer-Marschallinger, B., Bindlish, R., Wagner, W., Massari, C., 2020. Assimilation of Sentinel 1 and SMAP – based satellite soil moisture retrievals into SWAT hydrological model: the impact of satellite revisit time and product spatial resolution on flood simulations in small basins. J. Hydrol. 581, 124367 https://doi.org/10.1016/j.jhydrol.2019.124367.

Bladé, E., Cea, L., Corestein, G., Escolano, E., Puertas, J., Vázquez-Cendón, E., Dolz, J., Coll, A., 2014. Iber: herramienta de simulación numérica del flujo en ríos. Rev. Int. Metod. Numer. para Calc. y Disen. en Ing. 30, 1–10. https://doi.org/10.1016/j.rimni.2012.07.004.

Blöschl, G., Bierkens, M.F.P., Chambel, A., Cudennec, C., Destouni, G., Fiori, A., Kirchner, J.W., McDonnell, J.J., Savenije, H.H.G., Sivapalan, M., Stumpp, C., Toth, E., Volpi, E., Carr, G., Lupton, C., Salinas, J., Széles, B., Viglione, A., Aksoy, H., Allen, S.T., Amin, A., Andréassian, V., Arheimer, B., Aryal, S.K., Baker, V., Bardsley, E., Barendrecht, M.H., Bartosova, A., Batelaan, O., Berghuijs, W.R., Beven, K., Blume, T., Bogaard, T., Borges de Amorim, P., Böttcher, M.E., Boulet, G., Breinl, K., Brilly, M., Brocca, L., Buytaert, W., Castellarin, A., Castelletti, A., Chen, X., Chen, Y., Chen, Y., Chifflard, P., Claps, P., Clark, M.P., Collins, A.L., Croke, B., Dathe, A., David, P.C., de Barros, F.P.J., de Rooij, G., Di Baldassarre, G., Driscoll, J. M., Duethmann, D., Dwivedi, R., Eris, E., Farmer, W.H., Feiccabrino, J., Ferguson, G., Ferrari, E., Ferraris, S., Fersch, B., Finger, D., Foglia, L., Fowler, K., Gartsman, B., Gascoin, S., Gaume, E., Gelfan, A., Geris, J., Gharari, S., Gleeson, T., Glendell, M., Gonzalez Bevacqua, A., González-Dugo, M.P., Grimaldi, S., Gupta, A.B., Guse, B., Han, D., Hannah, D., Harpold, A., Haun, S., Heal, K., Helfricht, K., Herrnegger, M., Hipsey, M., Hlaváčiková, H., Hohmann, C., Holko, L., Hopkinson, C., Hrachowitz, M., Illangasekare, T.H., Inam, A., Innocente, C., Istanbulluoglu, E., Jarihani, B., Kalantari, Z., Kalvans, A., Khanal, S., Khatami, S., Kiesel, J., Kirkby, M., Knoben, W., Kochanek, K., Kohnová, S., Kolechkina, A., Krause, S., Kreamer, D., Kreibich, H., Kunstmann, H., Lange, H., Liberato, M.L.R., Lindquist, E., Link, T., Liu, J., Loucks, D.P., Luce, C., Mahé, G., Makarieva, O., Malard, J., Mashtayeva, S., Maskey, S., Mas-Pla, J., Mavrova-Guirguinova, M., Mazzoleni, M., Mernild, S., Misstear, B.D., Montanari, A., Müller-Thomy, H., Nabizadeh, A., Nardi, F., Neale, C., Nesterova, N., Nurtaev, B., Odongo, V.O., Panda, S., Pande, S., Pang, Z., Papacharalampous, G., Perrin, C., Pfister, L., Pimentel, R., Polo, M.J., Post, D., Prieto Sierra, C., Ramos, M.-H., Renner, M., Reynolds, J.E., Ridolfi, E., Rigon, R., Riva, M., Robertson, D.E., Rosso, R., Roy, T., Sá, J.H.M., Salvadori, G., Sandells, M., Schaefli, B., Schumann, A., Scolobig, A., Seibert, J., Servat, E., Shafiei, M., Sharma, A., Sidibe, M., Sidle, R.C., Skaugen, T., Smith, H., Spiessl, S.M., Stein, L., Steinsland, I., Strasser, U., Su, B., Szolgay, J., Tarboton, D., Tauro, F., Thirel, G., Tian, F., Tong, R., Tussupova, K., Tyralis, H., Uijlenhoet, R., van Beek, R., van der Ent, R.J., van der Ploeg, M., Van Loon, A.F., van Meerveld, I., van Nooijen, R., van Oel, P.R., Vidal, J.-P., von Freyberg, J., Vorogushyn, S., Wachniew, P., Wade, A.J., Ward, P., Westerberg, I.K., White, C., Wood, E.F., Woods, R., Xu, Z., Yilmaz, K.K., Zhang, Y., 2019. Twenty-three unsolved problems in hydrology (UPH) – a community perspective. Hydrol. Sci. J. 64, 1141–1158. https://doi.org/10.1080/02626667.2019.1620507.

Borgonovo, E., 2007. A new uncertainty importance measure. Reliab. Eng. Syst. Saf. 92, 771–784. https://doi.org/10.1016/j.ress.2006.04.015.

Brêda, J.P.L.F., Paiva, R.C.D., Bravo, J.M., Passaia, O.A., Moreira, D.M., 2019. Assimilation of Satellite Altimetry Data for Effective River Bathymetry. Water Resour. Res. 55, 7441–7463. https://doi.org/10.1029/2018WR024010.

Brocca, L., Melone, F., Moramarco, T., 2008. On the estimation of antecedent wetness conditions in rainfall–runoff modelling. Hydrol. Process. 22, 629–642. https://doi.org/10.1002/hyp.6629.

Cea, L., Bladé, E., 2015. A simple and efficient unstructured finite volume scheme for solving the shallow water equations in overland flow applications. Water Resour. Res. 51, 5464–5486. https://doi.org/10.1002/2014WR016547.

Cea, L., Garrido, M., Puertas, J., Jácome, A., Del Río, H., Suárez, J., 2010. Overland flow computations in urban and industrial catchments from direct precipitation data using a two-dimensional shallow water model. Water Sci. Technol. a. J. Int. Assoc. Water Pollut. Res. 62, 1998–2008. https://doi.org/10.2166/wst.2010.746.

Cea, L., Legout, C., Grangeon, T., Nord, G., 2016. Impact of model simplifications on soil erosion predictions: application of the GLUE methodology to a distributed event-based model at the hillslope scale. Hydrol. Process. 30, 1096–1113. https://doi.org/10.1002/hyp.10697.

Chow, V., Maidment, D.R., Mays, L.W., 1988. Applied Hydrology. Mc Graw Hill.

Costabile, P., Costanzo, C., 2021. A 2D-SWEs framework for efficient catchment-scale simulations: Hydrodynamic scaling properties of river networks and implications for non-uniform grids generation. J. Hydrol. 599, 126306 https://doi.org/10.1016/j.jhydrol.2021.126306.

Dasgupta, A., Hostache, R., Ramsankaran, R., Grimaldi, S., Matgen, P., Chini, M., Pauwels, V.R.N., Walker, J.P., 2021a. Chapter 12 - Earth Observation and Hydraulic Data Assimilation for Improved Flood Inundation Forecasting, en: Schumann, G.J.-P. B.T.-E.O. for F.A. (Ed.), Earth Observation. Elsevier, pp. 255-294. 10.1016/B978-0-12-819412-6.00012-2.

Dasgupta, A., Hostache, R., Ramsankaran, R., Schumann, G.J., Grimaldi, S., Pauwels, V. R.N., Walker, J.P., 2021b. On the impacts of observation location, timing, and frequency on flood extent assimilation performance. Water Resour. Res. 57 https://doi.org/10.1029/2020WR028238.

Dasgupta, A., Hostache, R., Ramsankaran, R., Schumann, G.J., Grimaldi, S., Pauwels, V. R.N., Walker, J.P., 2021c. A mutual information-based likelihood function for particle filter flood extent assimilation. Water Resour. Res. 57 https://doi.org/10.1029/2020WR027859.

Di Mauro, C., Hostache, R., Matgen, P., Pelich, R., Chini, M., van Leeuwen, P.J., Nichols, N.K., Blöschl, G., 2021. Assimilation of probabilistic flood maps from SAR data into a coupled hydrologic–hydraulic forecasting model: a proof of concept. Hydrol. Earth Syst. Sci. 25 (7), 4081–4097.

Di, C., Mauro, Hostache, R., Matgen, P., Pelich, R., Chini, M., van Leeuwen, P.J., Nichols, N.K., Bloschl, G., 2022. A tempered particle filter to enhance the assimilation of SAR derived flood extent maps into flood forecasting models. Water Resour. Res. https://doi.org/10.1002/essoar.10510211.1.

European Union Copernicus Land Monitoring Service, 2018. European Union. Copernicus Land Monitoring Service. Eur. Environ, Agency.

Ferraro, D., Costabile, P., Costanzo, C., Petaccia, G., Macchione, F., 2020. A spectral analysis approach for the a priori generation of computational grids in the 2-D hydrodynamic-based runoff simulations at a basin scale. J. Hydrol. 582, 124508 https://doi.org/10.1016/j.jhydrol.2019.124508.

Fraga, I., Cea, L., Puertas, J., 2013. Experimental study of the water depth and rainfall intensity effects on the bed roughness coefficient used in distributed urban drainage models. J. Hydrol. 505, 266–275. https://doi.org/10.1016/j.jhydrol.2013.10.005.

Fraga, I., Cea, L., Puertas, J., 2019. Effect of rainfall uncertainty on the performance of physically based rainfall–runoff models. Hydrological Processes 33 (1), 160–173.

García-Alén, G., González-Cao, J., Fernández-Nóvoa, D., Gómez-Gesteira, M., Cea, L., Puertas, J., 2022. Analysis of two sources of variability of basin outflow hydrographs computed with the 2D shallow water model Iber: Digital Terrain Model and unstructured mesh size. J. Hydrol. 612, 128182 https://doi.org/10.1016/j.jhydrol.2022.128182.

García-Feal, O., González-Cao, J., Gómez-Gesteira, M., Cea, L., Domínguez, J.M., Formella, A., 2018. An accelerated tool for flood modelling based on Iber. Water (Switzerland) 10, 1–23. https://doi.org/10.3390/w10101459.

Gavahi, K., Abbaszadeh, P., Moradkhani, H., Zhan, X., Hain, C., 2020. Multivariate assimilation of remotely sensed soil moisture and evapotranspiration for drought monitoring. J. Hydrometeorol. 21, 2293–2308. https://doi.org/10.1175/JHM-D-20-0057.1.

Giustarini, L., Matgen, P., Hostache, R., Montanari, M., Plaza, D., Pauwels, V.R.N., De Lannoy, G.J.M., De Keyser, R., Pfister, L., Hoffmann, L., Savenije, H.H.G., 2011. Assimilating SAR-derived water level data into a hydraulic model: a case study. Hydrol. Earth Syst. Sci. 15, 2349–2365. https://doi.org/10.5194/hess-15-2349-2011.

Herbst, E., Schorfheide, F., 2019. Tempered particle filtering. J. Econom. 210, 26–44. https://doi.org/10.1016/j.jeconom.2018.11.003.

Hostache, R., Chini, M., Giustarini, L., Neal, J., Kavetski, D., Wood, M., Corato, G., Pelich, R.-M., Matgen, P., 2018. Near-Real-Time Assimilation of SAR-Derived Flood Maps for Improving Flood Forecasts. Water Resour. Res. 54, 5516–5535. https://doi.org/10.1029/2017WR022205.

Hostache, R., Rains, D., Mallick, K., Chini, M., Pelich, R., Lievens, H., Fenicia, F., Corato, G., Verhoest, N.E.C., Matgen, P., 2020. Assimilation of Soil Moisture and Ocean Salinity (SMOS) brightness temperature into a large-scale distributed conceptual hydrological model to improve soil moisture predictions: the Murray-Darling basin in Australia as a test case. Hydrol. Earth Syst. Sci. 24, 4793–4812. https://doi.org/10.5194/hess-24-4793-2020.

IGN-CNIG, 2021. Instituto Geográfico Nacional [WWW Document]. Cent. Descargas del CNIG. URL http://centrodedescargas.cnig.es/CentroDescargas/index.jsp.

Jafarzadegan, K., Abbaszadeh, P., Moradkhani, H., 2021. Sequential data assimilation for real-time probabilistic flood inundation mapping. Hydrol. Earth Syst. Sci. 25, 4995–5011. https://doi.org/10.5194/hess-25-4995-2021.

Lievens, H., Reichle, R.H., Liu, Q., De Lannoy, G.J.M., Dunbar, R.S., Kim, S.B., Das, N.N., Cosh, M., Walker, J.P., Wagner, W., 2017. Joint Sentinel-1 and SMAP data assimilation to improve soil moisture estimates. Geophys. Res. Lett. 44, 6145–6153. https://doi.org/10.1002/2017GL073904.

Liu, Y., Gupta, H.V., 2007. Uncertainty in hydrologic modeling: Toward an integrated data assimilation framework. Water Resour. Res. 43 https://doi.org/10.1029/2006WR005756.

Matgen, P., Montanari, M., Hostache, R., Pfister, L., Hoffmann, L., Plaza, D., Pauwels, V. R.N., De Lannoy, G.J.M., De Keyser, R., Savenije, H.H.G., 2010. Towards the sequential assimilation of SAR-derived water stages into hydraulic models using the Particle Filter: proof of concept. Hydrol. Earth Syst. Sci. 14, 1773–1785. https://doi.org/10.5194/hess-14-1773-2010.

Meyer Oliveira, A., Fleischmann, A.S., Paiva, R.C.D., 2021. On the contribution of remote sensing-based calibration to model hydrological and hydraulic processes in tropical regions. J. Hydrol. 597, 126184 https://doi.org/10.1016/j.jhydrol.2021.126184.

Moradkhani, H., Hsu, K.-L., Gupta, H., Sorooshian, S., 2005. Uncertainty assessment of hydrologic model states and parameters: Sequential data assimilation using the particle filter. Water Resour. Res. 41 https://doi.org/10.1029/2004WR003604.

Moradkhani, H., Nearing, G.S., Abbaszadeh, P., Pathiraja, S., 2019. Fundamentals of data assimilation and theoretical advances. In: Duan, Q., Pappenberger, F., Wood, A., Cloke, H.L., Schaake, J.C. (Eds.), Handbook of Hydrometeorological Ensemble Forecasting. Springer Berlin Heidelberg, Berlin, Heidelberg, pp. 675–699.

Muñoz, D.F., Abbaszadeh, P., Moftakhari, H., Moradkhani, H., 2022. Accounting for uncertainties in compound flood hazard assessment: The value of data assimilation. Coast. Eng. 171, 104057 https://doi.org/10.1016/j.coastaleng.2021.104057.

Nguyen, P., Thorstensen, A., Sorooshian, S., Hsu, K., AghaKouchak, A., Sanders, B., Koren, V., Cui, Z., Smith, M., 2016. A high resolution coupled hydrologic–hydraulic model (HiResFlood-UCI) for flash flood modeling. J. Hydrol. 541, 401–420. https://doi.org/10.1016/j.jhydrol.2015.10.047.

Oubanas, H., Gejadze, I., Malaterre, P.-O., Mercier, F., 2018. River discharge estimation from synthetic SWOT-type observations using variational data assimilation and the full Saint-Venant hydraulic model. J. Hydrol. 559, 638–647. https://doi.org/10.1016/j.jhydrol.2018.02.004.

Peng, J., Albergel, C., Balenzano, A., Brocca, L., Cartus, O., Cosh, M.H., Crow, W.T., Dabrowska-Zielinska, K., Dadson, S., Davidson, M.W.J., de Rosnay, P., Dorigo, W., Gruber, A., Hagemann, S., Hirschi, M., Kerr, Y.H., Lovergine, F., Mahecha, M.D., Marzahn, P., Mattia, F., Musial, J.P., Preuschmann, S., Reichle, R.H., Satalino, G., Silgram, M., van Bodegom, P.M., Verhoest, N.E.C., Wagner, W., Walker, J.P., Wegmüller, U., Loew, A., 2021. A roadmap for high-resolution satellite soil moisture applications – confronting product characteristics with user requirements. Remote Sens. Environ. 252, 112162 https://doi.org/10.1016/j.rse.2020.112162.

Pettazzi, A., Salsón, S., 2012. Combining radar and rain gauges rainfall estimates using conditional merging: a case study, en: Seventh European Conference on Radar in Meteorology and Hydrology. Toulouse, France.

Reichle, R.H., De Lannoy, G.J.M., Liu, Q., Ardizzone, J.V., Colliander, A., Conaty, A., Crow, W., Jackson, T.J., Jones, L.A., Kimball, J.S., Koster, R.D., Mahanama, S.P., Smith, E.B., Berg, A., Bircher, S., Bosch, D., Caldwell, T.G., Cosh, M., González-Zamora, Á., Holifield Collins, C.D., Jensen, K.H., Livingston, S., Lopez-Baeza, E., Martínez-Fernández, J., McNairn, H., Moghaddam, M., Pacheco, A., Pellarin, T., Prueger, J., Rowlandson, T., Seyfried, M., Starks, P., Su, Z., Thibeault, M., van der Velde, R., Walker, J., Wu, X., Zeng, Y., 2017. Assessment of the SMAP Level-4 Surface and Root-Zone Soil Moisture Product Using In Situ Measurements. J. Hydrometeorol. 18, 2621–2645. https://doi.org/10.1175/JHM-D-17-0063.1.

Reichle, R., De Lannoy, G., Koster, R.D., Crow, W.T., Kimball, J.S., Liu, Q., 2020. SMAP L4 Global 3-hourly 9 km EASE-Grid Surface and Root Zone Soil Moisture Geophysical Data. Version 5, SPL4SMAU. https://doi.org/10.5067/9LNYIYOBNBR5.

Reichle, R.H., Liu, Q., Koster, R.D., Crow, W.T., De Lannoy, G.J.M., Kimball, J.S., Ardizzone, J.V., Bosch, D., Colliander, A., Cosh, M., Kolassa, J., Mahanama, S.P., Prueger, J., Starks, P., Walker, J.P., 2019. Version 4 of the SMAP Level-4 Soil Moisture Algorithm and Data Product. J. Adv. Model. Earth Syst. 11, 3106–3130. https://doi.org/10.1029/2019MS001729.

Revilla-Romero, B., Wanders, N., Burek, P., Salamon, P., de Roo, A., 2016. Integrating remotely sensed surface water extent into continental scale hydrology. J. Hydrol. 543, 659–670. https://doi.org/10.1016/j.jhydrol.2016.10.041.

Saltelli, A., 2002. Sensitivity analysis for importance assessment. Risk Anal. 22, 579–590. https://doi.org/10.1111/0272-4332.00040.

Sánchez, F.J., Lastra, J., 2011. Guía metodológica para el desarrollo del Sistema Nacional de Cartografía de Zonas Inundables. Medio Ambient. y Medio Rural y Mar, Madrid, Minist.

Sanz-Ramos, M., Bladé, E., González-Escalona, F., Olivares, G., Aragón-Hernández, J.L., 2021. Interpreting the Manning Roughness Coefficient in Overland Flow Simulations with Coupled Hydrological-Hydraulic Distributed Models. Water 13 (23), 3433.

Uber, M., Nord, G., Legout, C., Cea, L., 2021. How do modeling choices and erosion zone locations impact the representation of connectivity and the dynamics of suspended sediments in a multi-source soil erosion model? Earth Surf. Dynam. 9, 123–144. https://doi.org/10.5194/esurf-9-123-2021.

Van Leeuwen, P.J., Künsch, H.R., Nerger, L., Potthast, R., Reich, S., 2019. Particle filters for high-dimensional geoscience applications: A review. Q. J. R. Meteorol. Soc. 145, 2335–2365. https://doi.org/10.1002/qj.3551.

Wongchuig-Correa, S., Dias, C., de Paiva, R., Biancamaria, S., Collischonn, W., 2020. Assimilation of future SWOT-based river elevations, surface extent observations and discharge estimations into uncertain global hydrological models. J. Hydrol. 590, 125473 https://doi.org/10.1016/j.jhydrol.2020.125473.

Xu, L., Abbaszadeh, P., Moradkhani, H., Chen, N., Zhang, X., 2020. Continental drought monitoring using satellite soil moisture, data assimilation and an integrated drought index. Remote Sens. Environ. 250, 112028 https://doi.org/10.1016/j.rse.2020.112028.

Yan, H., Moradkhani, H., 2016. Combined assimilation of streamflow and satellite soil moisture with the particle filter and geostatistical modeling. Adv. Water Resour. 94, 364–378. https://doi.org/10.1016/j.advwatres.2016.06.002.